



# Coupled hygrothermal and mechanical simulations of highly anisotropic building material during freezing and thawing

Fukui, Kazuma  
Iba, Chiemi  
Ogura, Daisuke

---

**(Citation)**

Journal of Building Physics, 46(6):659-685

**(Issue Date)**

2023-05

**(Resource Type)**

journal article

**(Version)**

Accepted Manuscript

**(Rights)**

Fukui K, Iba C, Ogura D. Coupled hygrothermal and mechanical simulations of highly anisotropic building material during freezing and thawing. Journal of Building Physics. 2023;46(6):659-685. Copyright © The Author(s) 2023.  
doi:10.1177/17442591231165992

**(URL)**

<https://hdl.handle.net/20.500.14094/0100482054>



**Coupled hygrothermal and mechanical simulations of highly anisotropic building material during freezing and thawing**

**Kazuma Fukui<sup>1, \*</sup>, Chiemi Iba<sup>2</sup>, and Daisuke Ogura<sup>3</sup>**

<sup>1</sup> Assistant professor, Kobe University, Graduate School of Engineering, 1-1, Rokkodai-cho, Nada-ku, Kobe 657-8501, Japan

<sup>2</sup> Associate professor, Kyoto University, Kyoto 615-8540, Japan

<sup>3</sup> Professor, Kyoto University, Kyoto 615-8540, Japan

\*Corresponding author

Email: [fukui@peridot.kobe-u.ac.jp](mailto:fukui@peridot.kobe-u.ac.jp)

Phone: +81-78-803-6060

## 1 Nomenclature

### 2 Scalar

3	$a$	Coefficient related to the volumetric thermal expansion of pore volume occupied by each phase [ $\text{K}^{-1}$ ]
5	$c$	Specific heat [ $\text{J}/(\text{kg}\cdot\text{K})$ ]
6	$C$	Volumetric heat capacity of wet material [ $\text{J}/(\text{m}^3\cdot\text{K})$ ]
7	$E$	Young's modulus [Pa]
8	$E_{45}$	Young's modulus in the $45^\circ$ direction from the thickness direction [Pa].
9	$G$	Shear modulus [Pa]
10	$h$	Heat transfer coefficient between air and a material surface [ $\text{W}/(\text{m}^2\cdot\text{K})$ ]
11	$H$	Latent heat of solidification ( $334 \times 10^3 \text{ J/kg}$ )
12	$K$	Bulk modulus [Pa]
13	$m$	Mass of water contained in a unit volume of bulk material [ $\text{kg}/\text{m}^3$ ]
14	$N$	Biot tangent modulus [Pa]
15	$N_{ii}, N_{il}, N_{li},$ and $N_l$	Generalized Biot coupling modulus [Pa]
16	$p$	Pressure [Pa]
17	$S$	Saturation
18	$T$	Temperature [K],
19	$T_m$	Melting point of bulk water [K]
20	$T_{out}$	Air temperature [K]
21	$T_r$	Reference temperature [K]
22	$\alpha_\phi$	Coefficient related to the volumetric thermal expansion of pore volume [ $\text{K}^{-1}$ ]
23	$\gamma_{gl}$	Surface tension between air and liquid water [ $\text{N}/\text{m}$ ]
24	$\gamma_{li}$	Surface tension between liquid water and ice [ $\text{N}/\text{m}$ ]
25	$\Delta s$	Melting entropy ( $= 1.2 \text{ MPa/K}$ )
26	$\varphi$	Increment of the porosity
27	$\phi$	Porosity
28	$\phi_0$	Porosity in a reference state
29	$\nu$	Poisson's ratio
30	$\rho$	Density [ $\text{kg}/\text{m}^3$ ]
31	$\rho^0$	Density in a reference state [ $\text{kg}/\text{m}^3$ ]
32		
33	Tensor	
34	$\alpha$	Tensor of the coefficient of linear thermal expansion of a skeleton [ $\text{K}^{-1}$ ]
35	$\mathbf{b}$	Biot tangent tensor
36	$\mathbf{D}$	Elastic stiffness tensor [Pa]
37	$\mathbf{F}$	Body force vector [ $\text{N}/\text{m}^3$ ].
38	$\mathbf{J}$	Vectors of moisture flow [ $\text{kg}/(\text{m}^2\cdot\text{s})$ ]
39	$\mathbf{n}$	Unit vector normal to the surface
40	$\mathbf{Q}$	Vectors of heat flow [ $\text{W}/\text{m}^2$ ]
41	$\mathbf{t}$	External force vector [ $\text{N}/\text{m}^2$ ]
42	$\boldsymbol{\varepsilon}$	Strain tensor
43	$\boldsymbol{\lambda}$	Tensor of thermal conductivity [ $\text{W}/(\text{m}\cdot\text{K})$ ]
44	$\boldsymbol{\lambda}'$	Tensor of moisture permeability [ $\text{kg}/(\text{m}\cdot\text{s}\cdot\text{Pa})$ ]
45	$\boldsymbol{\sigma}$	Total stress tensor [Pa]
46		
47	Subscripts	
48	$d$	Bulk material in dry state
49	$g$	Water vapor
50	$i$	Ice
51	$n$	Direction normal to the thickness of a material
52	$l$	Liquid water

53 *s* Solid phase of a material  
54 *t* Directions along the thickness of a material

## 55 1. Introduction

56 The freezing of porous building materials is one of the main causes of deterioration in cold  
57 environments. Many studies have investigated freeze–thaw processes, damage risks, and mechanisms  
58 behind deformation and damage to predict deterioration, propose proper countermeasures, and create  
59 frost-resistant materials (Powers, 1945; Penttala, 1998; Scherer and Valenza II, 2005).

60 While numerous studies have experimentally investigated freeze-thaw resistance of building  
61 materials, e.g., (Fagerlund, 1997; Feng, et al., 2019), numerical simulations are considered an effective  
62 measure for addressing such challenges. To reveal freeze–thaw processes or evaluate frost damage  
63 risks, hygrothermal models for unsaturated materials have been successfully implemented to calculate  
64 the time evolution of temperature, liquid water content, and ice content distribution in building  
65 materials or walls (Hokoi, et al., 2000; Matsumoto, et al., 2001; Zhou, et al., 2017; Fukui, et al., 2021a).  
66 In addition, efforts have been made to develop a model with wider applications; Gawin et al. (2019)  
67 proposed a model that describes non-equilibrium freezing and hysteresis of the freezing and thawing.  
68 Moreover, based on the theory of poroelasticity (Biot, 1941) and poromechanics (Coussy, 2004),  
69 models have been developed and widely used to predict water pressure evolution and deformation in  
70 a material due to freezing (Coussy, 2005; Coussy & Monteiro, 2008; Wardeh and Perrin, 2008a;  
71 Wardeh, et al., 2010; Sun and Shcerer, 2010; Zeng, et al., 2013; Gong, et al., 2015), considering various  
72 mechanisms behind the development of water and ice pressure, such as pore-confined pressure,  
73 hydraulic pressure (Powers, 1945), cryosuction, and crystallization pressure (Scherer, 1999). These  
74 mechanical models do not consider heat and moisture movement in a material; therefore, they are used  
75 for sealed specimens, specimens with small size or low water permeability, or materials with entrained  
76 air in which water movement occurs locally due to sufficient pore space that allows the escape of pore  
77 water.

78 Among these models, coupling models of thermal and/or moisture transfer and mechanical  
79 behavior are considered powerful tools to reveal freeze–thaw processes and damage risks as well as  
80 to propose proper countermeasures under various environmental conditions and combination of  
81 material properties. Zuber and Marchand (2000) developed a hygro-mechanical model that was used  
82 by Wardeh and Perrin (2008b) to examine the causes of pressure development in fired clay materials  
83 during freezing. Zeng et al. (2011; 2016) used coupled hygrothermal and mechanical models to  
84 investigate the freeze–thaw processes of cement-based materials and supercooling effects. Recently,  
85 the applicability of such models has been enhanced to various problems, such as hysteresis in the  
86 freeze–thaw process (Koniarczyk, 2015), pore structure changes due to cyclic freezing and thawing  
87 (Koniarczyk, et al., 2015), and air-entrained effects (Eriksson, et al., 2018).

88 Porous building materials are often anisotropic, such as board materials, wood, stones, fired clay  
89 materials, and bio-based materials, because of their cellular or laminated structure; the anisotropy of  
90 transport properties and the strength of these materials have been investigated in the literature (Bech,  
91 et al., 2003; Nguyen, et al., 2016). As geomaterials, such as rocks and soils, also exhibit anisotropy  
92 either due to layered or microstructural characteristics, the theory of anisotropic poroelasticity has  
93 been developed to describe the mechanical behaviors of such materials. This theory was first  
94 developed by Biot (1955) and then examined by many researchers (Thompson and Willis, 1991;  
95 Cheng, 1997). This approach has also been applied to building materials. Rafsanjani et al. (2015)  
96 investigated the anisotropy of the swelling process of wood using a poromechanical model. Based on  
97 the theory of the anisotropic poroelasticity, the material strain is determined by Biot coefficient as well  
98 as stiffness tensor when the deformation is caused by pore pressure, i.e., swelling and drying, salt  
99 crystallization, freezing and thawing, and so on. Therefore, the consideration of the anisotropy of Biot  
100 coefficients is essential for the prediction of the stress and strain of anisotropic materials. However,  
101 the freeze–thaw processes of anisotropic porous building materials have not been sufficiently  
102 examined. As the poromechanical approach can potentially be applied for building wall scale (Moonen,  
103 et al., 2010; Koniarczyk & Gawin, 2012; Castellazzi, et al., 2013), the mechanical behaviors of

104 individual materials should be properly considered to understand their interactions with other materials  
 105 and behavior on a wall scale.

106 This study investigates prevalent numerical models for the coupled hygrothermal and mechanical  
 107 behaviors of anisotropic building materials during freezing and thawing. In a previous study (Fukui,  
 108 et al., 2021b), we conducted a parametric study to compare the calculation results with various  
 109 combinations of Biot coefficient values. In this study, the anisotropy of the Biot coefficient is further  
 110 investigated based on anisotropic poroelasticity, as well as consideration of anisotropy of the  
 111 mechanical properties. First, strain measurements are reported to demonstrate the anisotropy of  
 112 deformation during freezing and thawing using an ordinal brick and simulated roof tile, that have  
 113 strong anisotropy of material properties. Then the calculation model which corresponded to the  
 114 measurement was developed based on the conservation laws of the momentum, heat and moisture.  
 115 The model was based on the poromechanics theory and included the anisotropy of the mechanical and  
 116 poroelastic properties. The calculation results are then compared with the measurement results using  
 117 the roof tile; moreover, the impact of the anisotropy of each material property on the anisotropy of  
 118 deformation and the determinant of the magnitude of the deformation in each direction is investigated.

## 119 2. Theory of the anisotropic poroelasticity

120 After being established by Biot (1941), Biot himself extended the theory of poroelasticity to include  
 121 anisotropic materials (Biot, 1955). Later, the constitutive relations were reinterpreted and reformed  
 122 for easier application (Thompson and Willis, 1991; Cheng, 1997). In this study, the anisotropy of the  
 123 Biot coefficient is estimated according to the interpretation by Cheng (1997). This interpretation is  
 124 characterized by adopting micro-homogeneity and micro-isotropy assumptions to reduce the number  
 125 of independent parameters necessary for calculations, which means the skeleton of porous materials  
 126 is homogeneous and isotropic at microscopic scale. In the theory, the heterogeneity of the material can  
 127 be attributed to the distribution of the micro homogeneous constituents and its anisotropic can be  
 128 attributed to directional pores or fissure arrangement.

129 The generalized linear stress-strain relationship is

$$130 \quad \boldsymbol{\sigma} = \mathbf{D}\boldsymbol{\varepsilon} - \mathbf{b}p \quad (1)$$

131 After micromechanical analysis (for more details, see (Cheng, 1997; Abousleiman and Cui, 2000)),  
 132 the Biot tangent tensor for an orthotropic material can be expressed as

$$133 \quad b_1 = 1 - \frac{D_{11} + D_{12} + D_{13}}{3K_s}$$

$$134 \quad b_2 = 1 - \frac{D_{21} + D_{22} + D_{23}}{3K_s} \quad (2)$$

$$135 \quad b_3 = 1 - \frac{D_{31} + D_{32} + D_{33}}{3K_s}$$

136 Building materials and geomaterials are often transverse isotropic due to the pressing, laminating, or  
 137 deposition processes. For a material with its third-axis as the axis of rotational symmetry, assuming  
 138  $E_1 = E_2 = E$ ,  $E_3 = E'$ ,  $\nu_{12} = \nu$ , and  $\nu_{31} = \nu_{32} = \nu'$ :

$$139 \quad D_{11} = D_{22} = \frac{E(E' - E\nu'^2)}{(1 + \nu)(E' - E'\nu - 2E\nu'^2)}$$

$$140 \quad D_{12} = D_{21} = \frac{E(E'\nu - E\nu'^2)}{(1 + \nu)(E' - E'\nu - 2E\nu'^2)}$$

141 
$$D_{13} = D_{23} = \frac{EE'\nu'}{E' - E'\nu - 2E\nu'^2} \quad (3)$$

142 
$$D_{33} = \frac{E'^2(1-\nu)}{E' - E'\nu - 2E\nu'^2}$$

143 **3. Strain measurement**

144 In this section, the measurements are reported using a commercial brick and simulated roof tile.

145 *3.1. Methods*

146 Among other building materials, fired clay materials are susceptible to frost actions. To deal with the  
 147 increasing risks associated with the internal insulation of masonry walls intended to improve building  
 148 energy efficiency (Zhou, et al., 2017; Feng, et al., 2019) and to preserve historical tiles and bricks (Iba,  
 149 et al., 2016), it is becoming more and more important to understand the mechanisms behind  
 150 deformation and damage of fired clay materials due to frost actions. Moreover, these materials are  
 151 known to have anisotropic properties (Stolecki, et al., 1999) and anisotropy of the cracking due to the  
 152 freezing has been observed (Perrin, et al., 2011).

153 In this study, two fired clay materials are employed: commercial brick and simulated roof tile. The  
 154 bricks are made by a local manufacturer in Aichi Prefecture, Japan. The simulated roof tile is the same  
 155 as that used in our previous study (Fukui, et al., 2021a). The clay commonly used for producing roof  
 156 tiles in this area is sintered at a temperature of 1000 °C to prepare the simulated roof tile. The material  
 157 is not glazed or coated to avoid spoiling its homogeneity. In addition, because the material is thin, the  
 158 temperature distribution during the sintering is expected small, which also contributes to its  
 159 homogeneity than commercial bricks. Both materials are compressed along the thickness during the  
 160 shaping process; therefore, they are expected to exhibit anisotropic properties and be most deformable  
 161 along the thickness (Stolecki, et al., 1999). The logarithmic differential pore volume distributions of  
 162 the two materials obtained by mercury intrusion porosimetry are shown in Fig. 1. The peak of the pore  
 163 volume of the brick and simulated roof tile appears at the pore diameters of 8.5 and 0.14 μm,  
 164 respectively, which correspond to the freezing points of -0.015 and 0.9°C, respectively (Brun, et al.,  
 165 1977). Additionally, the basic material and mechanical properties are listed in Table 1, showing that  
 166 the mechanical properties of both the materials are strongly anisotropic.

167  
 168 [insert Figure 1]  
 169

170 **Table 1.** Mechanical and some basic material properties of the two kinds of fired clay materials.

Property		Commercial brick	Simulated roof tile
Dry density		1940 kg/m <sup>3</sup>	1800 kg/m <sup>3</sup>
Water content at vacuum saturation (regarded as porosity)		0.246 m <sup>3</sup> /m <sup>3</sup>	0.299 m <sup>3</sup> /m <sup>3</sup>
Young's modulus	$E_t$	$6 \times 10^9$ Pa	$3 \times 10^9$ Pa
	$E_n$	$19 \times 10^9$ Pa	$11 \times 10^9$ Pa
Poisson's ratio	$\nu_n$	0.14	0.12
	$\nu_{nt}$	0.44	0.44
	$\nu_{nn}$	0.32	0.19

171 \*Subscripts  $t$  and  $n$  represent the directions along and normal to the thickness, respectively.

172 A schematic of the strain measurement specimens is presented in Fig. 2. Specimens with the  
173 original material thickness (approximately 60 and 20 mm for the brick and simulated roof tile,  
174 respectively) are used. The specimens are rectangles with a bottom surface of 59.8 mm × 206.1 mm  
175 and 46.4 mm × 94.7 mm, and a height of 98.1 mm and 21.0 mm for the brick and simulated roof tile,  
176 respectively. The height of the specimen corresponds to the material thickness. Strain gauges and  
177 thermocouples are attached to the center of the top surface and to one of the 98.1 mm × 206.1 mm and  
178 21.0 mm × 94.7 mm sides of the commercial brick and roof tile specimens, respectively using  
179 cyanoacrylate adhesive. The strain gauges employed are KFLB-5-120-C1-11 R3M3 (Kyowa  
180 Electronic Instruments Co., Ltd). The strain is measured normal to and along the height on the top and  
181 side surfaces, respectively, to confirm the anisotropy of deformation during freezing and thawing. Due  
182 to the complexity to govern the equilibrium relationship among the three phases (air, liquid water, and  
183 ice) in the numerical simulations, the specimens were fully (vacuum-)saturated during the experiment  
184 for easier comparison. After attaching the strain gauges and thermocouples and saturating the  
185 specimen in a vacuum, the specimen is loosely covered with a thin plastic wrap to hinder surface  
186 vaporization but not to restrict the expansion of the specimen, allowing liquid water movement  
187 thorough the surfaces. The thermal resistance of the wrap is confirmed negligible prior to the  
188 experiment. The specimen is placed on a mesh to minimize thermal and mechanical interactions due  
189 to direct contact with the test chamber. In addition, the specimen is covered with a mesh basket to  
190 prevent direct exposure to the wind in the chamber.

191  
192 [insert Figure 2]

193  
194 To stabilize the distribution of the temperature in the specimen, the temperature of the air inside  
195 the test chamber with the specimen is first maintained at 20 °C for 30 min. The set temperature is then  
196 changed in a stepwise manner and maintained at -20 °C and 20 °C for 4 h during the cooling and  
197 heating periods, respectively, for the simulated roof tile. However, the minimum temperature is set to  
198 -10 °C for the commercial brick specimen due to the restrictions of experimental devices. From the  
199 pore volume distribution (shown in Fig. 1) and expected freezing temperature, this temperature is  
200 sufficient to freeze most of the pore water in the brick specimen. Considering the higher minimum  
201 temperature and larger dimensions of the commercial brick specimen, the cooling and heating periods  
202 are prolonged to 21 h and 15 h, respectively. The strain and temperature of the specimen are recorded  
203 every second during the experiment as well as the temperature of the air in the chamber.

### 204 3.2. Results

205 The measured time evolution of the temperature and strain of the specimens during the freeze-thaw  
206 experiments are shown in Figs. 3. Figure 4 displayed the measured strain changes as a function of the  
207 temperature. The strain evolutions on both the top and side surfaces (normal to and along the thickness,  
208 respectively) are presented in Figs. 3 and 4, but the temperature is not shown on the top surface in Fig.  
209 3 as the evolutions of temperature at the two measuring points are similar. The strain is shown referring  
210 to the values at 20 °C during the cooling process. In Fig. 3 (a), there is a sudden rise of the air  
211 temperature in the chamber at the elapsed time of 18 h due to open of the door of the test chamber to  
212 check the condition inside.

213  
214 [insert Figure 3]

215 [insert Figure 4]

216  
217 For the roof tile, the surface temperature once decreased to -4.8 °C and then suddenly increased  
218 due to the freezing of the supercooled water during an early stage of the cooling period. Then the  
219 measured temperature of both of the two materials stopped decreasing at sub-zero temperature due to  
220 the release of the latent heat. At the same time, the strain in the thickness direction of both of the  
221 materials start increasing.

222 The measurement results indicate that the strain along the thickness of both the materials  
223 significantly increases as the temperature decreases below 0 °C. In the direction normal to the

224 thickness, the commercial brick specimen contracts and then expands as the temperature decreased.  
 225 This expansion is faster than that along the thickness, but the magnitude is significantly smaller. After  
 226 the elapsed time of 12h, the increase of the strain in both directions stopped, which indicated most of  
 227 the freezable water solidified at this moment. From these results, the anisotropy of the deformation of  
 228 the brick due to the frost action was confirmed.

229 Moreover, the simulated roof tile demonstrates the stronger anisotropy of deformation due to frost  
 230 actions. It expanded more significantly in the thickness direction than the brick, but negligibly expands  
 231 in the direction normal to the thickness and rather contracts.

## 232 4. Numerical simulation

233 In this section, the hygrothermal and mechanical simulations are described based on the theory of  
 234 poromechanics. Herein, the simulated roof tile is selected as the object of calculation. The material  
 235 has a significantly strong anisotropy in its mechanical properties and simple dimensions, which allows  
 236 the use of a simple assumption in predicting the poroelastic properties that are not measured for general  
 237 building materials.

### 238 4.1. Methods

#### 239 4.1.1. Constitutive equations

240 Constitutive equations are based on the theory of poromechanics.

$$241 \quad \boldsymbol{\sigma} = \mathbf{D}[\boldsymbol{\varepsilon} - \boldsymbol{\alpha}(T - T_r)] - \mathbf{b}p \quad (4)$$

$$242 \quad \varphi = \mathbf{b} : \boldsymbol{\varepsilon} + \frac{p}{N} - \alpha_\phi(T - T_r) \quad (5)$$

243 When pores contain ice and liquid water, equations (4) and (5) are expressed as

$$244 \quad \boldsymbol{\sigma} = \mathbf{D}[\boldsymbol{\varepsilon} - \boldsymbol{\alpha}(T - T_r)] - (\mathbf{b}_i p_i + \mathbf{b}_l p_l) \quad (6)$$

$$245 \quad \varphi_i = \mathbf{b}_i : \boldsymbol{\varepsilon} + \frac{p_i}{N_{ii}} + \frac{p_l}{N_{il}} - a_i(T - T_r) \quad \varphi_l = \mathbf{b}_l : \boldsymbol{\varepsilon} + \frac{p_i}{N_{li}} + \frac{p_l}{N_{ll}} - a_l(T - T_r) \quad (7)$$

246 Coussy (2005) and Coussy & Monteiro (2008) expressed  $\mathbf{b}_i$  and  $\mathbf{b}_l$  in equations (6) and (7) as values  
 247 proportional to the ice and liquid water saturation, respectively, i.e.,

$$248 \quad \mathbf{b}_j = \mathbf{b}S_j \quad j = i, l \quad (8)$$

249 In addition, the anisotropy of  $\boldsymbol{\alpha}$  is ignored considering thermal effects on the deformation was not  
 250 significant compared with the water pressure development during the freezing; therefore, the thermal  
 251 expansion coefficient of the material is represented by one value,  $\alpha$ . The final forms of the constitutive  
 252 equations are  
 253

$$254 \quad \boldsymbol{\sigma} = \mathbf{D}[\boldsymbol{\varepsilon} - \alpha(T - T_r)\mathbf{I}] - \mathbf{b}(S_i p_i + S_l p_l) \quad (9)$$

$$255 \quad \varphi_i = S_i \mathbf{b} : \boldsymbol{\varepsilon} + \frac{p_i}{N_{ii}} + \frac{p_l}{N_{il}} - a_i(T - T_r) \quad \varphi_l = S_l \mathbf{b} : \boldsymbol{\varepsilon} + \frac{p_i}{N_{li}} + \frac{p_l}{N_{ll}} - a_l(T - T_r) \quad (10)$$



256 The poroelastic parameters  $a_j$ ,  $\mathbf{b}$ ,  $N_{ji}$ , and  $N_{jl}$  in equations (9) and (10) are to be given, but  $\mathbf{b}$  can be  
 257 calculated using equation (2) following the Cheng's assumption when  $K_s$  is obtained. As it is difficult  
 258 to fully determine the set of the poroelastic parameters from the measurement, we approximate these  
 259 values considering the strong anisotropy of the material. Considering the laminated structure of the  
 260 material, it is assumed to have parallel pores which were vertical to the thickness direction. This  
 261 assumption leads to a relationship  $E_s = E_n / (1 - \phi)$  and  $\nu_s = \nu_m$ .  $K_s$  is then obtained using the  
 262 relationship  $K_s = E_s / (3(1 - 2\nu_s))$ . Next, the equations derived by Aichi and Tokunaga (2011) are used  
 263 to obtain  $N_{ji}$  and  $N_{jl}$ . It is assumed that the Young's modulus along the thickness of the material is  
 264 significantly smaller than that in the direction normal to the thickness ( $E_t \ll E_n$ ) or that the deformation  
 265 in the normal direction is considerably smaller than that along the thickness. We obtain

$$266 \quad \frac{1}{N_{ll}} \approx \frac{b_l - \phi_0}{E_s} S_l^2 \quad \frac{1}{N_{il}} = \frac{1}{N_{li}} \approx \frac{b_l - \phi_0}{E_s} S_l S_i \quad \frac{1}{N_{ii}} \approx \frac{b_i - \phi_0}{E_s} S_i^2 \quad (11)$$

267 The derivation of  $a_j$  has not been reported for anisotropic materials in (Coussy, 2004). Since the  
 268 anisotropy of the thermal expansion coefficient of solid volume is ignored in this study, the thermal  
 269 expansion of pore volume is assumed to be isotropic. Therefore,  $a_j$  is derived assuming isotropy  
 270 (Coussy, 2004), as

$$271 \quad a_j = 3\alpha(b_l - \phi_0)S_j \quad j = i, l \quad (12)$$

272 Finally, the main simplifications used in the aforementioned equations can be summarized as follows:

- 273 • Plastic deformation of the material is ignored.
- 274 • As expressed in equation (8),  $\mathbf{b}_i$  and  $\mathbf{b}_l$  are set to values proportional to the saturation  $S$  (Coussy,  
 275 2005; Coussy and Monteiro, 2008).
- 276 • The anisotropy of the thermal expansion coefficient  $\alpha$  is ignored.
- 277 • The poroelastic parameters  $a_j$ ,  $N_{ji}$ , and  $N_{jl}$  are given in simplified forms. This is reasonable  
 278 because the simulated roof tile exhibits strong anisotropy.

#### 279 4.1.2. Equilibrium relationship between ice and liquid water

280 The Clausius–Clapeyron equation is expressed (Coussy and Monteiro, 2009) as

$$281 \quad \frac{p_l}{\rho_l} - \frac{p_i}{\rho_i} = \frac{\Delta s}{\rho_i} (T - T_m) \quad (13)$$

282 To express the dependencies of water density on the pressure  $p$  of each phase and temperature  $T$ ,  
 283 linearized form (Coussy, 2005; Coussy and Monteiro, 2008) is used as

$$284 \quad \frac{1}{\rho_j} = \frac{1}{\rho_j^0} \left( 1 - \frac{p_j}{K_j} + 3\alpha_j (T - T_r) \right) \quad j = i, l \quad (14)$$

285 Liquid water saturation  $S_l$  is obtained from the difference between ice pressure  $p_i$  and liquid water  
 286 pressure  $p_l$  under thermodynamic equilibrium conditions. The model as suggested by van Genuchten  
 287 (1980) is

$$288 \quad S_l = \left[ \frac{1}{1 + (\beta(p_i - p_l))^n} \right]^m \quad (15)$$

289 where  $m$ ,  $n$ , and  $\beta$  are fitting parameters.

290 The difference in the shape of the interface between ice and liquid water causes hysteresis during  
 291 freezing and thawing (Koniorczyk, et al., 2015; Gawin, et al., 2019). However, the freezing and

292 thawing processes are not distinguished in the calculation, i.e., the hysteresis is ignored, assuming that  
 293 it does not strongly affect the directionality of deformation.

#### 294 4.1.3. Conservation equations

295 The momentum balance and conservation equations for the heat and moisture mass are expressed as

$$296 \quad \nabla \cdot \boldsymbol{\sigma} + \mathbf{F} = 0 \quad (16)$$

$$297 \quad \frac{\partial}{\partial t}(CT - Hm_i) = \nabla \cdot (\boldsymbol{\lambda} \nabla T) \quad (17)$$

$$298 \quad \frac{\partial}{\partial t}(m_i + m_l) = \nabla \cdot (\boldsymbol{\lambda}' \nabla p_l) \quad (18)$$

299 where

$$300 \quad C = c_d \rho_d + c_i m_i + c_l m_l \quad (19)$$

301 Note that  $\mathbf{F} = 0$  because no source of the external force is considered

#### 302 4.1.4. Calculation model, numerical solution, and calculation conditions

303 Figure 5 presents the calculation model corresponding to the strain measurements described in the  
 304 previous section. The calculation is performed two-dimensionally to examine the relationship of the  
 305 strain in the two directions. The three-dimensional effects were not considered to reduce the  
 306 calculation cost given that the material is long and the heat and moisture transfer in the direction of  
 307 the long sides of the bottom surfaces is not dominant. The calculated region was on a quarter of a 40  
 308 mm  $\times$  20 mm cross-section (shown with a black square in Fig. 5), provided that the specimen is  
 309 symmetric. The direction of the 20-mm sides corresponds to the direction along the material thickness.  
 310 A plane-strain state is assumed as the strain in the depth direction was not significant. The  $x$ - and  $y$ -  
 311 axes of the rectangular coordinate system are set in the directions of the 40- and 20-mm sides,  
 312 respectively (shown in Fig. 5). The discretization of the conservation equations with respect to space  
 313 is performed using the Galerkin finite element method based on the monolithic approach, and 2 mm  
 314  $\times$  2 mm bilinear elements are used. The calculation results do not depend on the mesh size as confirmed  
 315 by comparing the calculation results using elements with half sides. Vectors of nodal values  $\mathbf{T}_e$ ,  $\mathbf{p}_e$ ,  
 316 and  $\mathbf{u}_e$  are used to express temperature  $T$ , liquid water pressure  $p_l$ , and displacement vector  $\mathbf{u}$ ,  
 317 respectively as well as the shape functions  $\mathbf{N}$  and  $\mathbf{N}_u$  as

$$318 \quad T = \mathbf{N} \mathbf{T}_e \quad p_l = \mathbf{N} \mathbf{p}_e \quad \mathbf{u} = \mathbf{N}_u \mathbf{u}_e \quad (20)$$

319 After discretization, the following system are obtained

$$320 \quad \begin{bmatrix} \mathbf{C}_{TT} & \mathbf{C}_{Tp} & \mathbf{C}_{Tu} \\ \mathbf{C}_{pT} & \mathbf{C}_{pp} & \mathbf{C}_{pu} \\ \mathbf{C}_{uT} & \mathbf{C}_{up} & \mathbf{C}_{uu} \end{bmatrix} \frac{\partial}{\partial t} \begin{bmatrix} \mathbf{T}_e \\ \mathbf{p}_e \\ \mathbf{u}_e \end{bmatrix} \\ = \begin{bmatrix} \mathbf{K}_{TT} & \mathbf{0} & \mathbf{0} \\ \mathbf{0} & \mathbf{K}_{uu} & \mathbf{0} \\ \mathbf{0} & \mathbf{0} & \mathbf{0} \end{bmatrix} \begin{bmatrix} \mathbf{T}_e \\ \mathbf{p}_e \\ \mathbf{u}_e \end{bmatrix} + \begin{bmatrix} \mathbf{f}_T \\ \mathbf{f}_p \\ \partial \mathbf{f}_u / \partial t \end{bmatrix} \quad (21)$$

321 where equation (16) is differentiated based on time. Components in equation (21) are presented in the  
 322 appendix. The finite difference method is used to discretize the basic equations with respect to time  
 323 with a backward difference. The time step is set to 1 s.

324

[insert Figure 5]

325

326

327

328

329

330

331

332

333

334

335

336

337

338

The initial and boundary conditions are listed in Table 2. The initial temperature of the material is set to a uniform value, and the average of the temperatures at the two measuring points at the beginning of the freeze–thaw experiment is used. The initial liquid water pressure  $p_l$  for the material is assumed to be 0 Pa as the specimen is vacuum saturated at the beginning of the experiment. On the symmetry axes ( $x = 0$  or  $y = 0$  in Fig. 5), the displacement is restricted normal to the axis directions and no heat or moisture flow is given. The surface vaporization is prevented by plastic wrap during the experiment; however, the wrap is not stiff and not considered to restrict movement of liquid water through the surfaces. Therefore, liquid water pressure  $p_l$  on the material surface is assumed to be 0 Pa. The heat flow through the surfaces is calculated using the Robin boundary condition and the measured air temperature in the test chamber. A stress-free boundary condition is assumed on the surfaces of the material. The thermal transfer coefficient  $h$  is set to 6.5 [W/(m<sup>2</sup>·K)] for the calculated temperature changes to agree with the measurement results.

339

**Table 2.** Initial and boundary conditions of the calculation.

	Position	Coordinates (shown in Fig. 5)	Heat	Moisture	Stress and displacement
Initial conditions	Calculation area	$0 \leq x \leq L_x$ and $0 \leq y \leq L_y$	Measured temperature	$p_l = 0$	$\mathbf{u} = 0$
Boundary conditions	Axes of symmetry	$x = 0$ or $y = 0$	$\mathbf{Q} \cdot \mathbf{n} = 0$	$\mathbf{J} \cdot \mathbf{n} = 0$	$\mathbf{u} \cdot \mathbf{n} = 0$
	Material surfaces	$x = L_x$ or $y = L_y$	$\mathbf{Q} \cdot \mathbf{n} = h (T - T_{out})$	$p_l = 0$	$\boldsymbol{\sigma} \cdot \mathbf{n} = 0$

340

#### 4.1.5. Hygrothermal and mechanical properties

341

342

343

344

345

The properties of the simulated roof tile with constant values necessary for the calculations, dry density, porosity, specific heat, thermal expansion coefficient, Young's modulus, and Poisson's ratio are listed in Table 3. The thermal expansion coefficient  $\alpha$  is determined from the slope of the strain as a function of the temperature above 0 °C in Fig. 4 (b). The table includes the anisotropy of the Young's modulus, and Poisson's ratio. The shear modulus  $G$  of the material is calculated as (Hayashi, 1954)

346

$$\frac{1}{G} = \frac{4}{E_{45}} - \left( \frac{1}{E_t} + \frac{1}{E_n} - \frac{\nu_m}{E_t} \right) \quad (22)$$

347

It is assumed that  $E_{45}$  is the average of  $E_t$  and  $E_n$ .

348 **Table 3.** Material properties of the simulated roof tile with constant values.

Property	Unit	Symbol	Value	Source
Dry density	kg/m <sup>3</sup>	$\rho_d$	1800	(Fukui, et al., 2021a)
Water content at vacuum saturation (regarded as porosity)	m <sup>3</sup> /m <sup>3</sup>	$\phi_0$	0.299	(Fukui, et al., 2021a)
Specific heat	J/(kg·K)	$c_d$	840	(Kumaran, 1996)
Thermal expansion coefficient	K <sup>-1</sup>	$\alpha$	$4.8 \times 10^{-6}$	Measurement
Young's modulus	Pa	$E_t$	$3 \times 10^9$	Measurement
		$E_n$	$11 \times 10^9$	Measurement
Poisson's ratio		$\nu_m$	0.12	Measurement
		$\nu_{nt}$	0.44	Measurement
		$\nu_{nn}$	0.19	Measurement

349 For simplicity, the anisotropy of the thermal conductivity is ignored as it does not significantly  
 350 affect the directionality of the deformation. Measurements are performed on specimens with various  
 351  $S_l$  values using the transient hot-wire method. From the results, the relationship between  $S_l$  and  $\lambda$   
 352 is obtained as (Fukui, et al., 2021a)

$$353 \quad \lambda = 1.26S_l + 0.55 \quad (23)$$

354 Additionally, the Maxwell equation, referring to de Vries (1963), is used to apply equation (23) to the  
 355 freezing and thawing processes as (Fukui, et al., 2021a)

$$356 \quad \lambda = 1.26S_l + 2.15S_i + 0.55 \quad (24)$$

357 Here the equation in the literature was rewritten using the saturation degree instead of the volumetric  
 358 water content.

359 The moisture retention curve of the material is obtained using the gas absorption and pressure plate  
 360 methods (Fukui, et al., 2021a). Figure 6(a) presents the measurement results and fitted curve. For the  
 361 fitted curve, the form suggested by van Genuchten (1980) is used as

$$362 \quad S_l = \left[ 1 + \left( \beta (p_g - p_l) \right)^n \right]^{-m} \quad (25)$$

363 The parameters in the equation are determined as follows:  $m = 0.57$ ,  $n = 2.3$ , and  $\beta = 1.12 \times 10^{-6} \text{ Pa}^{-1}$ .  
 364 Using the calibrated parameters, the liquid water saturation of the saturated material during freezing  
 365 and thawing is calculated considering the difference in the interfacial energy between the water vapor  
 366 and liquid water and between the liquid water and ice, as (Zeng, et al., 2011)

$$367 \quad S_l = \left[ 1 + \left( \beta' (p_i - p) \right)^n \right]^{-m} \quad (26)$$

368 where  $\beta' = (\gamma_{gl} / \gamma_{li}) \times \beta [\text{Pa}^{-1}]$ . As stated earlier, the hysteresis during the freeze–thaw processes is  
 369 ignored.

370  
 371 [insert Figure 6]  
 372

373 During the experiment, the water in the specimen is expected to move towards the surfaces from  
 374 the inside of the specimen due to the pressure development induced by freezing. Consequently, the  
 375 water pressure in the specimen can be relaxed to some extent. Therefore, the moisture transfer  
 376 properties of the material are considered important for predicting freezing strain. The water diffusivity  
 377  $D$  in the direction normal to the material thickness is obtained using the Boltzmann transformation

378 from time evolution of the water content distribution during water uptake measured using the gamma-  
 379 ray attenuation method (Fukui, 2021a). As the material is thin such that the moisture profile along the  
 380 thickness cannot be obtained using the same, mass measurements are performed during water uptake  
 381 to compare the average  $D$  (Kumaran 1999) along and normal to the thickness. From the results, the  
 382 average  $D$  is 2.1 times lesser along the thickness than in the direction normal to the thickness. Next,  
 383  $D$  in the entire saturation range is assumed 2.1 times smaller along the thickness. The  $\lambda'$  calculated  
 384 from  $D$  and the water retention curve are presented in Fig. 6 (b) along with the fitted curve.

#### 385 4.1.6. Poroelastic properties and calculation cases

386 The values of the Biot coefficient calculated from equation (2) with the Young's modulus and  
 387 Poisson's ratio listed in Table 3 are 0.679 and 0.219 along and normal to the thickness, respectively.  
 388 Therefore, not only the Young's modulus and Poisson's ratio but also the Biot coefficient of this  
 389 material are strongly anisotropic.

390 In equations (6) and (7), the anisotropy of the material strain is determined by the stiffness tensor  
 391 and Biot coefficient. Therefore, the anisotropy of the Young's modulus, Poisson's ratio, and Biot  
 392 coefficients has broad effects on the evolution of the material strain. The following three calculations  
 393 are conducted to examine the effects of each property.

- 394 • For Case 1, only the anisotropy of water permeability is considered.
- 395 • For Case 2, the anisotropy of Young's modulus and Poisson's ratio is considered as well as that  
 396 of the water permeability.
- 397 • For Case 3, the anisotropy of the Biot coefficient is considered as well as that of the water  
 398 permeability, Young's modulus, and Poisson's ratio.

399 These three cases are summarized in Table 4. When the isotropy of the Biot coefficients, Young's  
 400 modulus, and Poisson's ratio are assumed, the properties in the thickness directions are applied in all  
 401 the directions (values are provided in Table 3). Note that the anisotropy of the water permeability is  
 402 considered in all of the calculation cases because the property is related to the significance of the  
 403 pressure development and deformation, but the other material properties are assumed isotropic.

404 **Table 4** The consideration of anisotropic properties in each calculation case

	Young's modulus	Poisson's ratio	Biot coefficient
Case 1	Isotropy*	Isotropy*	Isotropy*
Case 2	Anisotropy	Anisotropy	Isotropy*
Case 3	Anisotropy	Anisotropy	Anisotropy

405 \*The properties in the thickness directions are applied in all directions.

#### 406 4.2. Results

407 Figures 7 and 8 present the results of the calculation of Case 1, as well as the measured temperature  
 408 and strain evolution, respectively. The strain evolution on both the top and side surfaces (normal to  
 409 and along the thickness, respectively) is presented in Fig. 8, but the temperature is not shown on the  
 410 top surface in Fig. 7 as the evolutions of temperature at the two measuring points are similar. Below  
 411 0 °C, the calculated strain along the thickness increases as the temperature decreases, same as the  
 412 measured strain. The difference in the magnitude of the calculated and measured evolutions of the  
 413 strain may be due to the inaccuracy in material properties, such as the moisture diffusivity and water  
 414 retention curve (These properties are related to the rate of the solidification and the water escape  
 415 toward the surfaces of the material due to the pressure development and consequently affect the  
 416 magnitude of the deformation. For example, smaller moisture diffusivity prevents moisture movement  
 417 when the pressure increases due to the freezing, which induces more significant pressure rise and strain.  
 418 Consequently, the agreement between the measurement and calculation will become better.) In  
 419 addition, the changes in the mechanical properties due to the water content changes (Fukui et al., 2019)

420 or evolution in the plastic strain can attribute to the difference between the measured and calculated  
 421 results. However, the trend in the measured strain change is well reproduced in the calculation.

422  
 423 [insert Figure 7]  
 424 [insert Figure 8]

425  
 426 For Case 1, the calculated strain in the direction normal to the thickness also increases and  
 427 completely disagrees with the measurement results that decrease during freezing. Therefore, the  
 428 mechanically and poroelastically isotropic models are insufficient for reproducing the measured  
 429 results.

430 Next, Figs 9 and 10 present the results of Cases 2 and 3. The calculated strain along the thickness  
 431 and the temperature do not significantly change from those in Case 1 (the temperature is not shown in  
 432 this paper). Although the strain change in the direction normal to the thickness during freezing in Case  
 433 2 (shown in Fig. 9) is smaller than that in Case 1, the material still expands in this direction. The  
 434 material contracts in this direction in Case 3 in which the anisotropy of the Biot coefficient is  
 435 considered, which is consistent with the measured results.

436  
 437 [insert Figure 9]  
 438 [insert Figure 10]  
 439

#### 440 4.3. Discussion

441 In this section we compare the contribution of the temperature changes, water pressure development,  
 442 and Poisson's effects to the strain evolution based on the calculation results where the anisotropy of  
 443 the Young's modulus, Poisson's ratio, and Biot coefficient is considered, and analyze the dominant  
 444 sources of the deformation in each direction of the material. First, thermal contraction due to the  
 445 temperature changes during the freeze-thaw cycle along and normal to the thickness is determined  
 446 based on the calculated temperature evolution as

$$447 \quad \varepsilon_u^T = \varepsilon_m^T = \alpha(T - T_r) \quad (27)$$

448 Here we ignored the anisotropy of the thermal expansion coefficient.  $T_r$  is the set value of the initial  
 449 temperature (20 °C). Next, the strain change due to water (liquid water and ice) pressure development  
 450 in the material (excluding Poisson's effects) is obtained based on the calculated ice and liquid water  
 451 saturation and pressure as

$$452 \quad \varepsilon_u^H = \frac{b_t}{E_t}(S_i p_i + S_l p_l) \quad \varepsilon_{nm}^H = \frac{b_n}{E_n}(S_i p_i + S_l p_l) \quad (28)$$

453 Finally, the Poisson's effects due to the expansion associated with water pressure development in the  
 454 vertical direction are considered as

$$455 \quad \varepsilon_u^P = -\frac{v_m b_n}{E_t}(S_i p_i + S_l p_l) \quad \varepsilon_{nm}^P = -\frac{v_{nt} b_t}{E_n}(S_i p_i + S_l p_l) \quad (29)$$

456 As no external force was considered in the calculations, these three factors are main determinant of  
 457 the deformation of the material.

458 Using equations (27) to (29) with the calculated temperature, water saturation, and pressure  
 459 evolution in Case 3, the strain due to the thermal contraction, hydrostatic pressure, and Poisson's  
 460 effect were calculated. Figure 11 shows comparison of the contribution of these causes of the  
 461 deformation to the strain evolution. Due to the restriction of the deformation from the neighborhood  
 462 elements, the sum of the strain caused by the three causes is not consistent perfectly with the calculated  
 463 overall strain shown in Fig. 10. However, it seems that they mainly determine the magnitude and trend

464 of the deformation. From Fig. 11 (a), the expansion along the thickness is mainly attributed to the  
 465 increase in the hydrostatic pressure in the material due to freezing; moreover, the thermal contraction  
 466 and Poisson's effects are almost negligible. In contrast, Fig. 11 (b) shows that the three components  
 467 of strain evolution compete in the direction normal to the thickness. The expansion associated with  
 468 the hydrostatic pressure development is suppressed due to the small Biot coefficient and large Young's  
 469 modulus in this direction, while the Poisson's effect is dominant because of the large expansion along  
 470 the thickness. According to these results, the contribution of the water pressure rise in pores to the  
 471 deformation of the specimen is relatively small in the direction normal to the thickness compared with  
 472 the contribution of the Poisson effect accompanied by the expansion along the thickness. This resulted  
 473 in the contraction of the material in the direction normal to the thickness. Therefore, a model that only  
 474 considers the anisotropy of the general mechanical properties (Case 2) cannot reproduce such a  
 475 contraction, and the anisotropy of the Biot coefficients should be adequately considered.

476  
 477 [insert Figure 11]  
 478

## 479 5. Conclusion

480 In this study, the effects of anisotropy of the material properties on the deformation during freezing  
 481 and thawing processes and proper numerical modeling of it are investigated. The strain measurement  
 482 using two fired clay materials confirmed the strongly anisotropic deformation during the freezing.  
 483 Notably, the plate-shaped simulated roof tile contracted in the direction normal to the thickness while  
 484 it expanded significantly in the thickness direction. The freeze–thaw process is then simulated based  
 485 on theory of poromechanics and anisotropic poroelasticity. The comparison between the measured and  
 486 calculated results reveals that applying only the anisotropy of mechanical properties is insufficient for  
 487 reproducing the anisotropic deformation of the material; moreover, the contraction in the direction  
 488 normal to the thickness can be reproduced only when the anisotropies of the Biot coefficient and  
 489 general mechanical properties are considered. Analysis of the causes of the deformation reveals that  
 490 the expansion in the direction normal to the thickness due to the pressure development during the  
 491 freezing is suppressed by the large Young's modulus and small Biot coefficient and the contraction  
 492 due to the Poisson's effects accompanied by the large expansion in the thickness direction can be a  
 493 dominant factor of the deformation in the direction normal to the thickness. Therefore, considering the  
 494 anisotropy of the Biot coefficient is recommended when materials with laminated structures, such as  
 495 types of stones and fired clay materials, are considered.

496 In this study, we chose the simulated roof tile as the target of the calculations considering its  
 497 relatively simple dimensions, small heterogeneity, and strong anisotropy in the mechanical properties  
 498 due to the laminated structure or orientation of particles compared with bricks, which allowed us to  
 499 predict the poroelastic properties under simple assumptions of parallel pore structure. In the future,  
 500 the deformation of bricks, which also exhibited the anisotropy in the strain measurement will be further  
 501 explored for the practical application. In addition, the validity of such assumptions for other types of  
 502 building materials needs further investigation for a wider application of anisotropic poroelasticity to  
 503 various building materials

## 504 Appendix

505 The components in equation (21) are defined as

$$506 \quad \mathbf{C}_{TT} = \int_{\Omega} \frac{\partial}{\partial T} (CT - H_i m_i) \mathbf{N}^T \mathbf{N} d\Omega \quad (\text{A.1})$$

$$507 \quad \mathbf{C}_{Tp} = \int_{\Omega} \frac{\partial}{\partial p_i} (CT - H m_i) \mathbf{N}^T \mathbf{N} d\Omega \quad (\text{A.2})$$

$$508 \quad \mathbf{C}_{\mathbf{T}\mathbf{u}} = \int_{\Omega} \frac{\partial}{\partial \varepsilon_v} (CT - Hm_i) \mathbf{N}^T \mathbf{m}^T \mathbf{B} d\Omega \quad (\text{A.3})$$

$$509 \quad \mathbf{C}_{\mathbf{p}\mathbf{T}} = \int_{\Omega} \frac{\partial}{\partial T} (m_i + m_l) \mathbf{N}^T \mathbf{N} d\Omega \quad (\text{A.4})$$

$$510 \quad \mathbf{C}_{\mathbf{p}\mathbf{p}} = \int_{\Omega} \frac{\partial}{\partial p_l} (m_i + m_l) \mathbf{N}^T \mathbf{N} d\Omega \quad (\text{A.5})$$

$$511 \quad \mathbf{C}_{\mathbf{p}\mathbf{u}} = \int_{\Omega} \frac{\partial}{\partial \varepsilon_v} (m_i + m_l) \mathbf{N}^T \mathbf{m}^T \mathbf{B} d\Omega \quad (\text{A.6})$$

$$512 \quad \mathbf{C}_{\mathbf{u}\mathbf{T}} = - \int_{\Omega} \left[ \alpha \mathbf{B}^T \mathbf{D} + b \frac{\partial}{\partial T} (S_i p_i + S_l p_l) \mathbf{B}^T \right] \mathbf{m} \mathbf{N} d\Omega \quad (\text{A.7})$$

$$513 \quad \mathbf{C}_{\mathbf{u}\mathbf{p}} = - \int_{\Omega} b \frac{\partial}{\partial p_l} (S_i p_i + S_l p_l) \mathbf{B}^T \mathbf{m} \mathbf{N} d\Omega \quad (\text{A.8})$$

$$514 \quad \mathbf{C}_{\mathbf{u}\mathbf{u}} = \int_{\Omega} \mathbf{B}^T \mathbf{D} \mathbf{B} d\Omega \quad (\text{A.9})$$

$$515 \quad \mathbf{K}_{\mathbf{T}\mathbf{T}} = \int_{\Omega} \nabla \mathbf{N}^T \lambda \nabla \mathbf{N} d\Omega + \int_{\Gamma} h \mathbf{N}^T d\Gamma \quad (\text{A.10})$$

$$516 \quad \mathbf{K}_{\mathbf{p}\mathbf{p}} = \int_{\Omega} \nabla \mathbf{N}^T \lambda' \nabla \mathbf{N} d\Omega \quad (\text{A.11})$$

$$517 \quad \mathbf{f}_{\mathbf{T}} = - \int_{\Gamma} (Q - hT_{out}) \mathbf{N}^T d\Gamma \quad (\text{A.12})$$

$$518 \quad \mathbf{f}_{\mathbf{p}} = - \int_{\Gamma} J \mathbf{N}^T d\Gamma \quad (\text{A.13})$$

$$519 \quad \frac{\partial \mathbf{f}_{\mathbf{u}}}{\partial t} = \frac{\partial}{\partial t} \int_{\Gamma} \mathbf{N}_{\mathbf{u}}^T \mathbf{t} d\Gamma \quad (\text{A.14})$$

520 where  $\Omega$  and  $\Gamma$  are the domains of an element and its boundary, respectively; moreover,

$$521 \quad \mathbf{m} = [1 \quad 1 \quad 0]^T \quad (\text{A.15})$$

$$522 \quad \mathbf{B} = \begin{bmatrix} \frac{\partial N_1}{\partial x_1} & 0 & \frac{\partial N_2}{\partial x_1} & 0 & \frac{\partial N_3}{\partial x_1} & 0 & \frac{\partial N_4}{\partial x_1} & 0 \\ 0 & \frac{\partial N_1}{\partial x_2} & 0 & \frac{\partial N_2}{\partial x_2} & 0 & \frac{\partial N_3}{\partial x_2} & 0 & \frac{\partial N_4}{\partial x_2} \\ \frac{\partial N_1}{\partial x_2} & \frac{\partial N_1}{\partial x_1} & \frac{\partial N_2}{\partial x_2} & \frac{\partial N_2}{\partial x_1} & \frac{\partial N_3}{\partial x_2} & \frac{\partial N_3}{\partial x_1} & \frac{\partial N_4}{\partial x_2} & \frac{\partial N_4}{\partial x_1} \end{bmatrix} \quad (\text{A.16})$$

523



524

**References**

- 525 Abousleiman, Y. & Cui, L., 2000. The theory of anisotropic poroelasticity with applications. In:  
526 *Modeling in Geomechanics*. New York: Wiley, pp. 559-93.
- 527 Aichi, M. & Tokunaga, T., 2011. Thermodynamically consistent anisotropic constitutive relations for  
528 a poroelastic material saturated by two immiscible fluids. *International Journal of Rock Mechanics*  
529 *& Mining Sciences*, Volume 48, pp. 580-84.
- 530 Bech, K., Al-Mukhtar, M., Rozenbaum, O. & Rautureau, M., 2003. Characterization, water transfer  
531 properties and deterioration in tuffeau: building material in the Loire valley—France. *Building and*  
532 *Environment*, Volume 38, pp. 1152-62.
- 533 Biot, M. A., 1941. General theory of three-dimensional consolidation. *Journal of Applied Physics*,  
534 Volume 12, pp. 155-64.
- 535 Biot, M. A., 1955. Theory of elasticity and consolidation for a porous anisotropic solid. *Journal of*  
536 *Applied Physics*, Volume 26, pp. 182-85.
- 537 Brun, M., Lallemand, A., Quinson, J. & Eyraud, C., 1977. A new method for the simultaneous  
538 determination of the size and the shape of pores: the thermoporometry. *Thermochimica Acta*,  
539 Volume 21, pp. 59-88.
- 540 Castellazzi, G. et al., 2013. A coupled multiphase model for hygrothermal analysis of masonry  
541 structures and prediction of stress induced by salt crystallization. *Construction and Building*  
542 *Materials*, Volume 41, pp. 717-31.
- 543 Cheng, A. H.-D., 1997. Material coefficients of anisotropic poroelasticity. *International Journal of*  
544 *Rock Mechanics & Mining Sciences*, Volume 34, pp. 199-205.
- 545 Coussy, O., 2004. *Poromechanics*. s.l.:John Wiley & Sons.
- 546 Coussy, O., 2005. Poromechanics of freezing materials. *Journal of the Mechanics and Physics of Solids*,  
547 Volume 53, pp. 1689-1718.
- 548 Coussy, O. & Monteiro, P. J., 2008. Poroelastic model for concrete exposed to freezing temperatures.  
549 *Cement and Concrete Research*, Volume 38, pp. 40-48.
- 550 Coussy, O. & Monteiro, P. J., 2009. Errata to 'Poroelastic model for concrete exposed to freezing  
551 temperatures'. *Cement and Concrete Research*, Volume 39, pp. 371-72.
- 552 de Vries, D. A., 1963. Thermal properties of soils. In: *Physics of Plant Environment*. Amsterdam:  
553 North-Holland Publishing Corporation, pp. 210-35.
- 554 Eriksson, D., Gasch, T., Malm, R. & Ansell, A., 2018. Freezing of partially saturated air-entrained  
555 concrete: A multiphase description of the hygro-thermo-mechanical behaviour. *International*  
556 *Journal of Solids and Structures*, Volume 152-53, pp. 294-304.
- 557 Fagerlund, G., 1997. *Internal frost attack-state of the art: suggestions for future research (Report*  
558 *TVBM (Intern 7000-rapport); Vol. 7110)*, Division of Building Materials, LTH, Lund University.
- 559 Feng, C., Roels, S. & Janssen, H., 2019. Towards a more representative assessment of frost damage  
560 to porous building materials. *Building and Environment*, Volume 164, p. 106343.
- 561 Fukui, K. et al., 2021a. Investigation into the hygrothermal behavior of fired clay materials during the  
562 freezing of supercooled water using experiments and numerical simulations. *Journal of Building*  
563 *Physics*, p. <https://doi.org/10.1177/17442591211041144>.
- 564 Fukui, K., Chiemi, I., Daisuke, O., 2021b. Effects of anisotropy of properties of fired clay materials  
565 on strain evolution and results of coupled hygrothermal and mechanical simulations during  
566 freezing and thawing. In: *8th International Building Physics Conference*, Copenhagen, Denmark,  
567 25-27 August 2021.
- 568 Gawin, D., Pesavento, F., Koniorczyk, M. & Schrefler, B. A., 2019. Non-equilibrium modeling  
569 hysteresis of modeling hysteresis of thawing in partially saturated porous building materials.  
570 *Journal of Building Physics*, Volume 43, pp. 61-98.
- 571 Gong, F., Sicat, E., Zhang, D. & Ueda, T., 2015. Stress analysis for concrete materials under multiple  
572 freeze-thaw cycles. *Journal of Advanced Concrete Technology*, Volume 13, pp. 124-34.
- 573 Hayashi, T., 1954. On the elastic properties of an orthogonal-anisotropic plate having the principal axes  
574 of elasticity slanted to its edges. *Journal of the Japan Society of Aeronautical Engineering*, Volume 2,  
575 pp. 12-17.
- 576 Hokoi, S., Hatano, M., Matsumoto, M. & Kumaran, M. K., 2000. Freezing-Thawing Processes in  
577 Glass Fiber Board. *Journal of Thermal Envelope and Building Science*, Volume 24, pp. 42-60.

578 Iba, C., Ueda, A. & Hokoi, S., 2016. Field survey on frost damage to roof tiles under climatic  
579 conditions. *Structural Survey*, Volume 34, pp. 135-49.

580 Koniorczyk, M., 2015. Coupled heat and water transport in deformable porous materials considering  
581 phase change kinetics. *International Journal of Heat and Mass Transfer*, Volume 81, pp. 260-71.

582 Koniorczyk, M. & Gawin, D., 2012. Modelling of salt crystallization in building materials with  
583 microstructure - Poromechanical approach. *Construction and Building Materials*, Volume 36, pp.  
584 860-73.

585 Koniorczyk, M., Gawin, D. & Schrefler, B. A., 2015. Modeling evolution of frost damage in fully  
586 saturated porous materials exposed to variable hygro-thermal conditions. *Computer Methods in  
587 Applied Mechanics and Engineering*, Volume 297, pp. 38-61.

588 Kumaran, M. K., 1996. *IEA Annex 24, Final Report, Vol. 3, Task 3: Material Properties*. Leuven:  
589 Laboratorium Boufysica, Department Burgerlijke Bouwkunde, KU Leuven.

590 Kumaran, M. K., 1999. Moisture diffusivity of building materials from water absorption measurements.  
591 *Journal of Thermal Envelope and Building Science*, Volume 22, pp. 349-55.

592 Penttala, V., 1998. Freezing-induced strains and pressures in wet porous materials

593 Matsumoto, M., Hokoi, S. & Hatano, M., 2001. Model for simulation of freezing and thawing  
594 processes in building materials. *Building and Environment*, Volume 36, pp. 733-42.

595 Moonen, P., Sluys, L. J. & Carmeliet, J., 2010. A continuous-discontinuous approach to simulate  
596 physical degradation process in porous media. *International Journal for Numerical Methods in  
597 Engineering*, Volume 84, pp. 1009-37.

598 Nguyen, S. T. et al., 2016. Modeling thermal conductivity of hemp insulation material: A multi-scale  
599 homogenization approach. *Building and Environment*, Volume 107, pp. 127-34.

600 Penttala, V., 1998. Freezing-induced strains and pressures in wet porous materials and especially in  
601 concrete mortars. *Advanced Cement Based Materials*, Volume 7, pp. 8-19.

602 Perrin, B. et al., 2011. Mechanical behaviour of fired clay materials subjected to freeze-thaw cycles.  
603 *Construction and Building Materials*, Volume 25, pp. 1056-64.

604 Powers, T. C., 1945. A working hypothesis for further studies of frost resistance of concrete. *Journal  
605 of the American Concrete Institute*, Volume 16, pp. 245-72.

606 Rafsanjani, A., Derome, D. & Carmeliet, J., 2015. Poromechanical modeling of moisture induced  
607 swelling anisotropy in cellular tissues of softwoods. *RSC Advances*, Volume 5, pp. 3560-66.

608 Scherer, G. W., 1999. Crystallization in pores. *Cement and Concrete Research*, Volume 29, pp. 1347-  
609 58.

610 Scherer, G. W. & Valenza II, J. J., 2005. Mechanisms of frost damage. In: *Materials Science of  
611 Concrete VII*. s.l.:American Ceramic Society, pp. 209-46.

612 Stolecki, J., Piekarczyk, J. & Rudnik, T., 1999. Heterogeneity and anisotropy of ceramic roof tiles.  
613 *British Ceramic Proceedings*, Volume 60, pp. 383-84.

614 Sun, Z. & Sheerer, G. W., 2010. Effects of air voids on salt scaling and internal freezing. *Cement and  
615 Concrete Research*, Volume 40, pp. 260-70.

616 Thompson, M. & Willis, J. R., 1991. A reformation of the equations of anisotropic poroelasticity.  
617 *Journal of Applied Mechanics*, Volume 58, pp. 612-16.

618 Van Genuchten, M. T., 1980. A Closed-form Equation for Predicting the Hydraulic Conductivity of  
619 Unsaturated Soils. *Soil Science Society of America Journal*, Volume 44, pp. 892-98.

620 Wardeh, G., Mohamed, M. A. & Ghorbel, E., 2010. Analysis of concrete internal deterioration due to  
621 frost action. *Journal of Building Physics*, Volume 35, pp. 54-82.

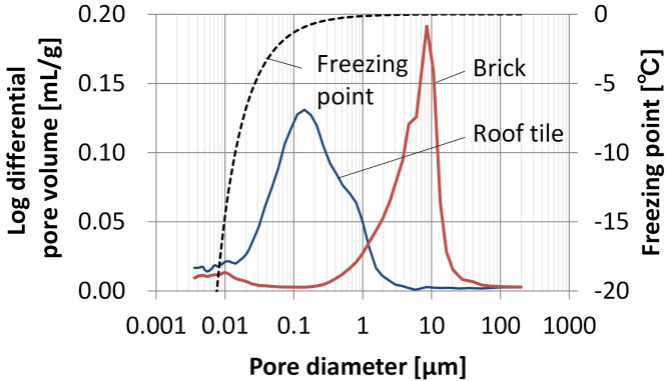
622 Wardeh, G. & Perrin, B., 2008a. Numerical modelling of the behaviour of consolidated porous media  
623 exposed to frost action. *Construction and Building Materials*, Volume 22, pp. 600-08.

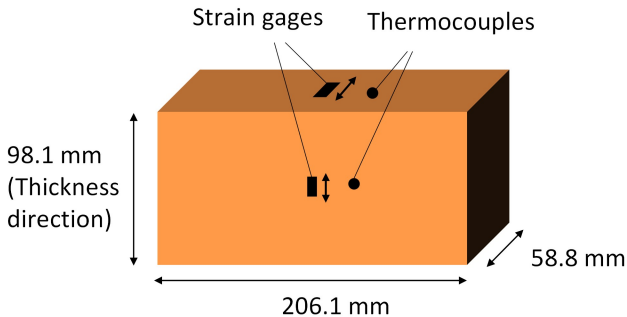
624 Wardeh, G. & Perrin, B., 2008b. Freezing-thawing phenomena in fired clay materials and  
625 consequences on their durability. *Construction and Building Materials*, Volume 22, pp. 820-28.

626 Zeng, Q., Fen-Chong, T., Dangla, P. & Li, K., 2011. A study of freezing behavior of cementitious  
627 materials by poromechanical approach. *International Journal of Solids and Structures*, Volume 48,  
628 pp. 3267-73.

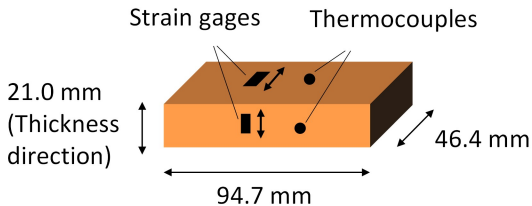
629 Zeng, Q., Fen-Chong, T. & Li, K., 2013. Elastic behavior of saturated porous materials under  
630 undrained freezing. *Acta Mechanica Sinica*, Volume 29, pp. 827-35.

- 631 Zeng, Q., Li, K. & Fen-Chong, T., 2016. Effect of supercooling on the instantaneous freezing dilation  
632 of cement-based porous materials. *Journal of Building Physics*, Volume 40, pp. 101-24.
- 633 Zhou, X., Derome, D. & Carmeliet, J., 2017. Hygrothermal modeling and evaluation of freeze-thaw  
634 damage risk of masonry walls retrofitted with internal insulation. *Building and Environment*,  
635 Volume 125, pp. 285-98.
- 636 Zuber, B. & Marchand, J., 2000. Modeling the deterioration of hydrated cement systems exposed to  
637 frost action Part 1: Description of the mathematical model. *Cement and Concrete Research*,  
638 Volume 30, pp. 1929-39.  
639

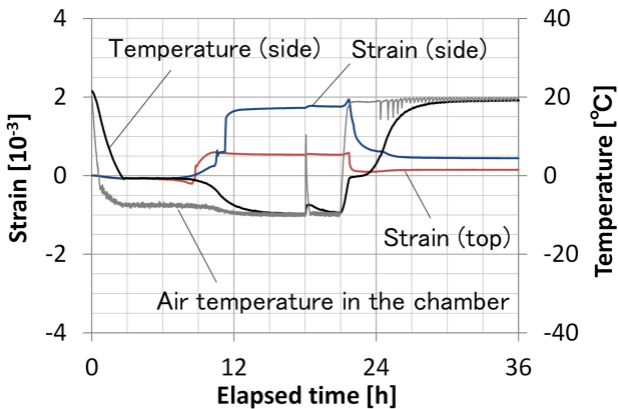




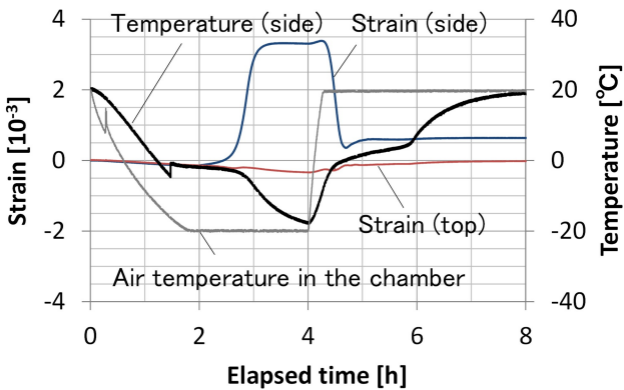
(a)



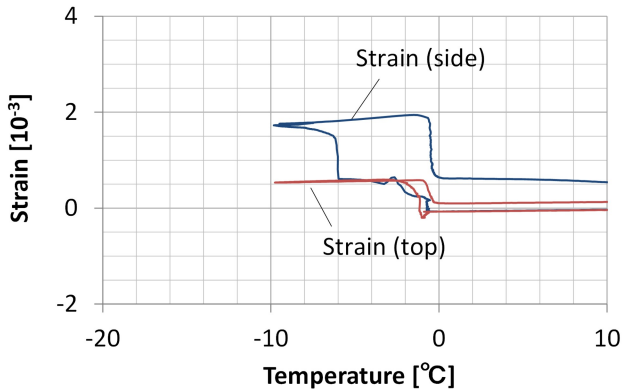
(b)



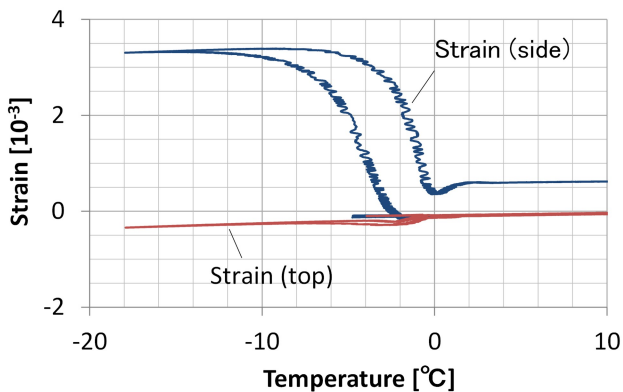
(a)



(b)

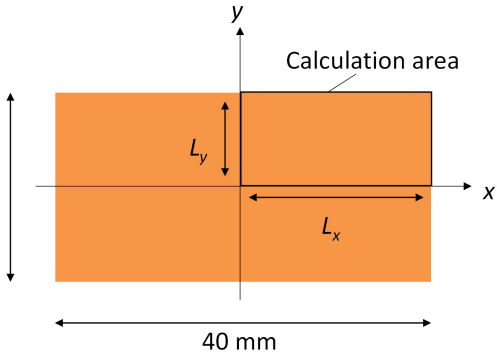


(a)

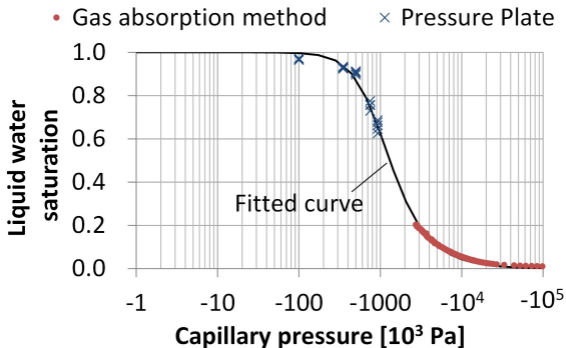


(b)

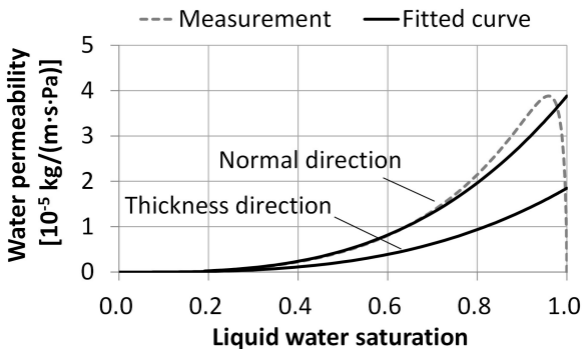
20 mm  
(Height direction)





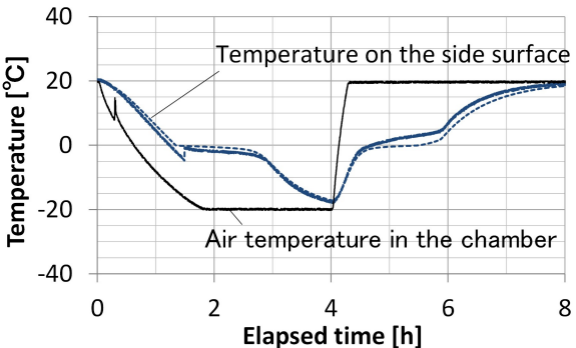


(a)

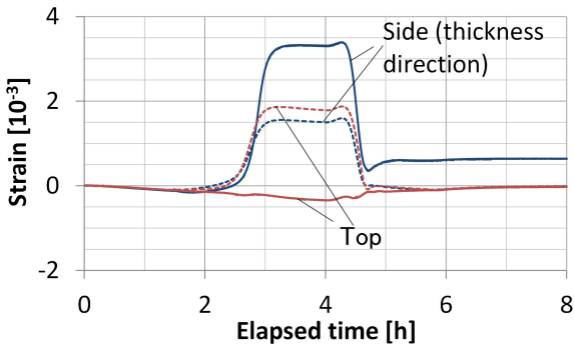


(b)

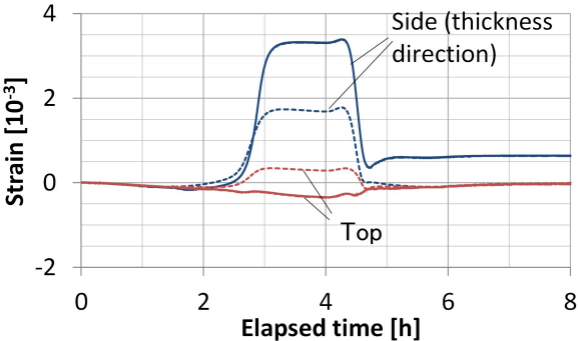
Solid lines: experiment; Dotted lines: calculation



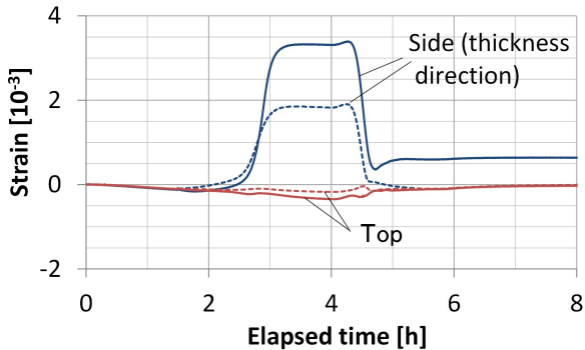
Solid lines: experiment; Dotted lines: calculation



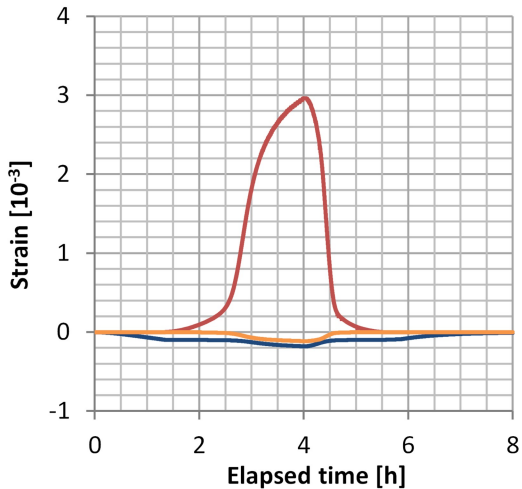
Solid lines: experiment; Dotted lines: calculation



Solid lines: experiment; Dotted lines: calculation

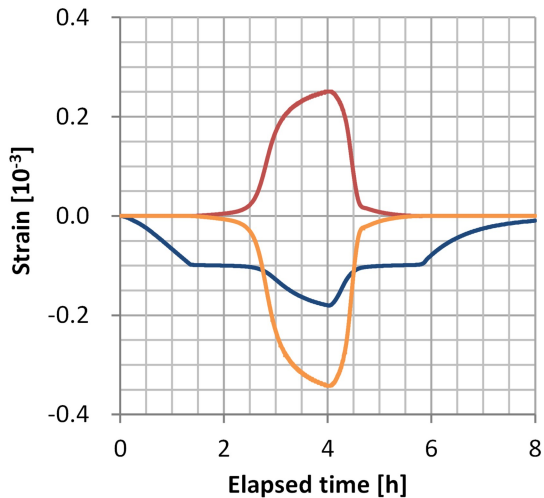


— Thermal contraction  
— Pore pressure  
— Poisson's effect



(a)

— Thermal contraction  
— Pore pressure  
— Poisson's effect



(b)